Chemical Science

ROYAL SOCIETY OF CHEMISTRY

EDGE ARTICLE

View Article Online
View Journal | View Issue

Cite this: *Chem. Sci.*, 2022, **13**, 1335

All publication charges for this article have been paid for by the Royal Society of Chemistry

Received 4th November 2021
Accepted 13th January 2022

DOI: 10.1039/d1sc06131c

rsc.li/chemical-science

2D-C_3N_4 encapsulated perovskite nanocrystals for efficient photo-assisted thermocatalytic CO_2 reduction†

Hui Bian,[a] Deng Li,[a] Shengyao Wang,[c] Junqing Yan *[a] and Shengzhong (Frank) Liu *[ab]

Very recently, halide perovskites, especially all-inorganic $CsPbBr_3$, have received ever-increasing attention in photocatalysis owing to their superior optoelectronic properties and thermal stability. However, there is a lack of study on their application in thermocatalysis and photo-thermocatalysis. Herein, we rationally designed a core–shell heterojunction formed by encapsulating $CsPbBr_3$ nanoparticles with the 2D C_3N_4 (m-CN) layer *via* a solid-state reaction (denoted as m-CN@$CsPbBr_3$). A series of experiments suggest that abundant adsorption and active sites of CO_2 molecules as well as polar surfaces were obtained by utilizing m-CN-coated $CsPbBr_3$, resulting in significant improvement in CO_2 capture and charge separation. It is found that the m-CN@$CsPbBr_3$ effectively drives the thermocatalytic reduction of CO_2 in H_2O vapor. By coupling light into the system, the activity for CO_2-to-CO reduction is further improved with a yield up to 42.8 μmol g^{-1} h^{-1} at 150 °C, which is 8.4 and 2.3 times those of pure photocatalysis (5.1 μmol g^{-1} h^{-1}) and thermocatalysis (18.7 μmol g^{-1} h^{-1}), respectively. This work expands the application of general halide perovskites and provides guidance for using perovskite-based catalysts for photo-assisted thermocatalytic CO_2 reduction.

The reduction of CO_2 into valuable hydrocarbon fuels *via* chemical catalytic processes to mitigate the greenhouse-effect has received wide attention.[1,2] Basically, the CO_2 molecule has a straight double-bonded non-polar structure, resulting in a huge activation energy barrier for the CO_2 reduction reaction (CRR).[3,4] Using a catalyst to adsorb and then activate the CO_2 molecules with free electrons is thus imperative.[5,6] Currently, there are three main types of catalytic CO_2 reduction reactions, *i.e.* thermocatalysis,[7] electrocatalysis[8a,b] and photocatalysis,[4b,c,5c] where the catalysts used are referred to as thermocatalysts, electrocatalysts and photocatalysts, respectively. Traditionally, thermocatalysis is regarded as the conventional CRR process where the CO_2 molecules are well-activated and reduced by thermocatalysts using heat and the reductant agent H_2. Hence, thermocatalysis usually shows a relatively higher CRR efficiency compared to the other two cases.[7a,b,9a] However, as it is very complex to safely transport and use H_2 for this process, it is more advantageous to use safe and free H_2O as the reductant if high thermocatalytic CRR efficiency can be achieved. Photocatalysis is regarded as an effective approach for CO_2 reduction owing to the merits of utilizing solar energy directly and low energy consumption. However, the efficiency of the photocatalytic CRR is still limited by the sluggish kinetics of CO_2 activation and H_2O dissolving.[4c,9b] Very recently, Xu and co-workers reported a novel lead-free perovskite, $Cs_3Sb_2I_9$, for CO_2 reduction to CO and CH_4 *via* photothermal synergistic catalysis without using any sacrificial agents or cocatalysts.[9c] Unfortunately, the perovskite is not stable enough in the working solution. In addition, its activity is still limited. There is still some room to develop a simple method for synthesizing effective and stable photothermal catalysts.

All-inorganic perovskites, for example cesium lead tribromide ($CsPbBr_3$), have emerged as a promising type of photocatalyst for the CRR, owing to their long photogenerated carrier diffusion length, tunable size, wide light-absorption range, *etc.*[5c,10] $CsPbBr_3$ perovskites have been widely explored in composites with other materials, such as g-C_3N_4,[11] graphene oxide[5a,12] and TiO_2 (ref. 13) to construct heterojunctions for photocatalytic CO_2 reduction. For example, Xu and his co-workers mixed $CsPbBr_3$ with NH_x-rich g-C_3N_4 nanosheets to construct a heterojunction with a fast carrier-transfer bridge for improved charge separation and hence enhanced photocatalytic activity for CO_2 reduction.[14a] Similarly, Lu's group reported the coating of $CsPbBr_3$ with graphdiyne as a physical

[a]Key Laboratory of Applied Surface and Colloid Chemistry, Shaanxi Engineering Lab for Advanced Energy Technology, School of Materials Science and Engineering, Shaanxi Normal University, Xi'an 710119, China. E-mail: junqingyan@snnu.edu.cn
[b]Dalian National Laboratory for Clean Energy, Dalian Institute of Chemical Physics, Chinese Academy of Sciences, Dalian 116023, China. E-mail: szliu@dicp.ac.cn
[c]College of Science, Huazhong Agricultural University, Wuhan 430070, P. R. China

† Electronic supplementary information (ESI) available. See DOI: 10.1039/d1sc06131c

protection layer to tackle the stability issue in photocatalytic CO_2 reduction in H_2O vapor, given that the perovskite shows a low tolerance towards water.[14b] It should be mentioned that most of the reported halide perovskite nanocrystals (NCs) were prepared by the solution method using organic solvents, which is troublesome for large-scale production.[15a,b] Besides, considering that thermocatalysis usually outperforms photocatalysis in CO_2 reduction, it would be intriguing to explore the catalytic activity of $CsPbBr_3$ under coupled thermal and irradiation effects. To the best of our knowledge, there are few reports of water-stable $CsPbBr_3$-based thermal CRR with H_2O as a reducing agent.

Herein, using a molten-salt method, we elaborately encapsulate $CsPbBr_3$ with a 2D m-CN layer to construct a water-stable heterojunction for photo-assisted thermal catalytic CO_2 reduction. We found that under pure thermocatalysis conditions, m-CN@$CsPbBr_3$ showed the ability to drive the CRR reduction to CO using the CO_2 and H_2O as reactants. Moreover, with the introduction of simulated solar illumination, the corresponding reduction yield rises to 42.8 μmol g^{-1} h^{-1}, which is 2.3 and 8.4 times those of pure thermocatalysts and photocatalysts, respectively. This is the first report on the fabrication of $CsPbBr_3$ perovskite NCs by means of a solid-phase reaction. This work expands the application of $CsPbBr_3$ perovskite and can help us better understand CO_2 reduction by H_2O.

A molten-salt method, where ion salts act as a high-temperature liquid solvent to accelerate the dissolution of raw materials, the transport of reactants, and the directional assembly of basic units, was used to prepare perovskite catalysts with a specific morphology.[15c] It is worth noting that melem can be obtained by thermal condensation of urea below 450 °C, while g-C_3N_4 can be acquired in the temperature range between 480 °C and 550 °C (Fig. S1a†).[16a] Therefore, the composition of the coating layer may be assigned to an intermediate product (named m-CN) possessing many edge NH_x groups between melem and g-C_3N_4, which is attributed to the higher local temperature (>450 °C) caused by the molten salt. To confirm this, a comparison study is performed at 420 °C and 470 °C for the synthesis of m-CN@$CsPbBr_3$ catalysts. As revealed in Fig. S1b,† the best preparation temperature is 450 °C for m-CN@$CsPbBr_3$ catalysts, while the phase transition of $CsPbBr_3$ occurs at 470 °C. During the heat treatment, $CsPbBr_3$ was changed into the solution state, *i.e.* molten salt (Fig. S2†). Meanwhile the polymerized monomers of carbon nitride adsorbed onto the surface of $CsPbBr_3$, and then the micron-sized $CsPbBr_3$ was "cut" into nanoparticles by encapsulation with m-CN coatings, as shown in Fig. 1a. To elucidate the formation process of m-CN@$CsPbBr_3$, different coatings with $CsPbBr_3$-to-urea mass ratios of 1 : 3, 1 : 5 and 1 : 10 were synthesized and are denoted as m-CN@$CsPbBr_3$-3, m-CN@$CsPbBr_3$-5 and m-CN@$CsPbBr_3$-10, respectively. The corresponding XRD and FTIR results also suggest the encapsulation of $CsPbBr_3$ with m-CN in these samples, as shown in Fig. S3a and b.† It should be noted that the m-CN@$CsPbBr_3$-3 sample gives the typical peaks of g-C_3N_4 at 2-theta of 13 and 27°, while the broad XRD peaks of m-CN@$CsPbBr_3$-10 could be ascribed to melem, suggesting that a certain content of molten

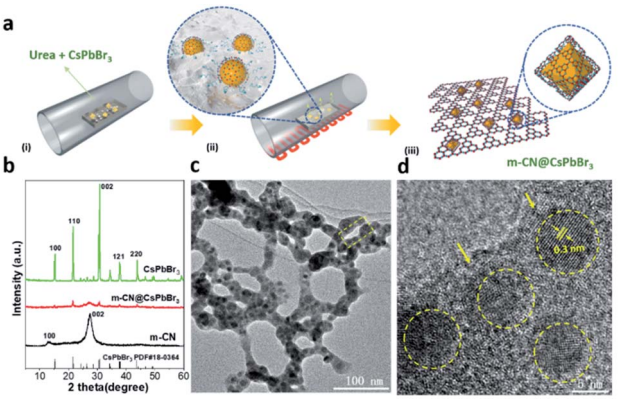

Fig. 1 (a) Illustration of the synthesis of m-CN@$CsPbBr_3$; (b) XRD patterns of m-CN@$CsPbBr_3$, the reference m-CN and $CsPbBr_3$; (c and d) TEM image and the corresponding HRTEM result of m-CN@$CsPbBr_3$, where the yellow arrows mark the thin m-CN layers.

salt is required to improve the temperature profile for the thermal polymerization of the CN coating layers.[16b] Fourier transform infrared (FTIR) spectroscopy of m-CN@$CsPbBr_3$-3 and m-CN@$CsPbBr_3$-10 showed similar peaks, where the peaks in the wide range from 1200 to 1700 cm^{-1} are attributed to the skeleton signal of g-C_3N_4.[16c] The absorption bands from 3000 to 3500 cm^{-1} come from NH_x and –OH groups.[14a,16b] In comparison to m-CN@$CsPbBr_3$-10, the normalized intensity of the band from 3000 to 3500 cm^{-1} for m-CN@$CsPbBr_3$-3 is evidently decreased, which can be ascribed to the stronger interactions of edge NH_x groups and bromide anions of $CsPbBr_3$.[16] It is also observed that the m-CN@$CsPbBr_3$-3 peaks shifted to lower values compared with m-CN@$CsPbBr_3$-10, as shown in the magnified FTIR spectra of Fig. S3,† suggesting stronger interactions occurred with the introduction of more bromide anions.[14a,16d] When the relative mass ratio of urea to $CsPbBr_3$ is changed, either the amount of loaded $CsPbBr_3$ particles is lower and sporadic (Fig. S4a,† m-CN@$CsPbBr_3$-10) or the $CsPbBr_3$ particles are larger and exposed (Fig. S4b,† m-CN@$CsPbBr_3$-3), whereas the m-CN@$CsPbBr_3$-5 sample displays completely uniform and coated $CsPbBr_3$ particles, suggesting that the appropriate ratio of urea to $CsPbBr_3$ is critical for optimal m-CN@$CsPbBr_3$ formation. Therefore, the m-CN@$CsPbBr_3$-5 catalyst with an optimized coating ratio was chosen for further study because it may be endowed with a more heterogeneous interface and excellent stability. For the synthesis of pure $CsPbBr_3$ for further composition, vacuum was employed to obtain less-defective $CsPbBr_3$. We also attempted to treat the mixture of $CsPbBr_3$ and urea in air. However, very little polymerization of urea to carbon nitride occurred, and thus, the N_2 condition was chosen for m-CN@$CsPbBr_3$ preparation. Therefore, we successfully encapsulated the perovskite $CsPbBr_3$ with a 2D m-CN layer by utilizing $CsPbBr_3$ as a molten salt under N_2 conditions. It is greatly emphasized that this is the first report on the fabrication of $CsPbBr_3$ perovskite NCs by means of a solid-phase reaction. Differing from the traditional synthesis approaches such as ball milling and solution processing strategies, this unique method can avoid some difficulties, including

a complicated procedure and the formation of organic branches and undesired phases, showing the attractive application of this method for fabricating catalysts beyond perovskites.

As a representative material, m-CN@$CsPbBr_3$-5 is selected to investigate the influence of encapsulating perovskite nanocrystals with 2D m-CN for boosting photo-assisted thermocatalytic CO_2 reduction. The XRD patterns in Fig. 1b show that the intensity of the peaks ascribed to $CsPbBr_3$ was obviously decreased after the m-CN encapsulation, suggesting that the crystallinity of $CsPbBr_3$ is reduced. Magnification of the diffraction region from 21.2 to 22° suggests that the m-CN@$CsPbBr_3$ sample exhibits a larger full-width at half maximum (FWHM) than bare $CsPbBr_3$ (Fig. S5†), further indicating that the particle size was decreased by the calcination treatment. It should also be noted that the as-prepared $CsPbBr_3$ formed in a vacuum also showed a crystal-lattice orientation, given that the texture coefficient of the [200] peak is much higher than the standard value of 1, while it is less than 1 for $CsPbBr_3$ prepared in N_2 and air (Fig. S6a and b†). It is noted that the texture coefficient of the [200] peak is in agreement with $CsPbBr_3$ prepared in N_2 after m-CN coating, which further proved the melt-crystallization process of $CsPbBr_3$. The FTIR spectra of m-CN@$CsPbBr_3$ and melem showed similar peaks (Fig. S7†), and the normalized intensity of the band from 3000 to 3500 cm^{-1} of m-CN@$CsPbBr_3$ is obviously decreased compared to the reference m-CN. Furthermore, compared with the pure m-CN layer, the peaks for m-CN@$CsPbBr_3$ located at 1250 cm^{-1}, corresponding to the typical stretching mode of aromatic C–N and C=N heterocycles in m-CN, are systematically shifted to lower values in the magnified FTIR spectra in Fig. S7,† suggesting that the edge NH_x groups interact with the bromide anion of $CsPbBr_3$ *via* ionic bonding.[16,17a] Fig. 1c displays the transmission electron microscopy (TEM) image of the m-CN@$CsPbBr_3$ sample. Clearly, it shows that the $CsPbBr_3$ nanoparticles were uniformly encapsulated by the m-CN layer. The corresponding high-resolution transmission electron microscopy (HRTEM) images further show clear lattice fringes with a measured interplanar spacing of 0.3 nm, as shown in Fig. 1d, which can be assigned to the (002) plane of cubic $CsPbBr_3$. Additionally, it shows that nano-sized (*ca.* 8 nm) $CsPbBr_3$ particles were encapsulated by the m-CN layer in the m-CN@$CsPbBr_3$ catalyst (Fig. S8†). In contrast, the reference $CsPbBr_3$, which was prepared without urea, is micron-sized (Fig. S9†), further confirming that the particle size of $CsPbBr_3$ was changed by the *in situ* encapsulation with the m-CN layer. Fig. S10† displays the scanning transmission electron microscopy (STEM) image with the corresponding elemental mapping results, which further confirm that the $CsPbBr_3$ nanoparticles are wrapped by the m-CN layer. The TEM images and the corresponding elemental mapping of the reference synthesized melem are shown in Fig. S11 and S12,† respectively, and they resemble those of m-CN@$CsPbBr_3$, further confirming that the coating layer can be attributed to m-CN.

X-ray photoelectron spectroscopy (XPS) was carried out to study the chemical environment of the elements in the m-CN@$CsPbBr_3$ heterojunction. Fig. S13a† shows the C 1s XPS results of m-CN@$CsPbBr_3$ and reference m-CN samples. Two main peaks located at *ca.* 284.8 and 288.2 eV can be detected, and the first is assigned to the C–C in graphitic carbon, while the second comes from the N–C=N coordination of triazine rings.[16,17b] It should be noted that there is a slight shift of the N–C=N signal of m-CN@$CsPbBr_3$ to higher binding energy as compared with the bare m-CN, indicating there is an interaction between $CsPbBr_3$ and m-CN. For the corresponding N 1s XPS curves, three main peaks centered at 398.7, 399.7 and 400.9 eV can be detected (Fig. S13b†), and they can be assigned to C–N=C, N–$(C)_3$ and C–N–H of the carbon nitride skeleton, respectively.[17] However, the weak peak at *ca.* 404.4 eV is usually regarded as coming from positive charge localization in heterocycles.[17c] It almost disappears in m-CN@$CsPbBr_3$ relative to bare m-CN, further suggesting that there is some chemical interaction between m-CN and $CsPbBr_3$ for neutralizing the positive charge.[14a] Fig. S14a† gives the Cs 3d XPS results of m-CN@$CsPbBr_3$ and bare $CsPbBr_3$. Two main peaks at 724.5 and 738.4 eV can be detected and come from the Cs $3d_{5/2}$ and $3d_{3/2}$ signals.[14,15] However, a slight shift to higher binding energy can be detected for m-CN@$CsPbBr_3$, further confirming the above mutual interaction between m-CN and $CsPbBr_3$. In the Pb 4f XPS result in Fig. S14b,† there are two peaks at *ca.* 138.4 and 143.3 eV. Similarly, there is a shift to higher binding energy for m-CN@$CsPbBr_3$ compared with $CsPbBr_3$. Fig. S14c† shows the Br 3d XPS results. Clearly, there are two fitted peaks located at *ca.* 68.3 and 69.3 eV. The sample of m-CN@$CsPbBr_3$ exhibits a *ca.* 0.2 eV shift to higher binding energy compared with bare $CsPbBr_3$. Both the shifts of Pb 4f and Br 3d in the XPS results suggest that chemical bonds of N–Br have been formed during the preparation process.[11b,14a]

The UV-vis absorption spectra of the pristine m-CN and micro-sized $CsPbBr_3$ in Fig. 2a exhibit the typical absorption edges of $CsPbBr_3$ and m-CN at *ca.* 553 and 430 nm, corresponding to bandgaps of 2.24 and 2.88 eV, respectively. For the sample of m-CN@$CsPbBr_3$, two obvious edges were observed, which correspond to the light absorption edges of $CsPbBr_3$ and m-CN, indicating the successful combination of the two materials. Fig. S15† displays the photoluminescence (PL) curves from 375 nm excitation. Strong emission at *ca.* 450 nm was marked for m-CN, and the peak at 524 nm is attributed to $CsPbBr_3$. There are two peaks in the PL curve of m-CN@$CsPbBr_3$, confirming the composition of the catalyst. Moreover, compared with the bare m-CN and $CsPbBr_3$, the PL intensity of m-CN@$CsPbBr_3$ is lower, which indicates suppressed carrier recombination in m-CN@$CsPbBr_3$. The time-resolved PL spectrum was further obtained to explore the carrier dynamics of m-CN@$CsPbBr_3$. Fig. S16a and b† exhibit the transient PL spectra at 440 and 523 nm, where the signals can be considered as coming from m-CN and $CsPbBr_3$ (Fig. S15†), respectively, and the corresponding fitted results are shown in Tables S1 and S2.† Obviously, compared with pure m-CN at 440 nm (Fig. S16a†), m-CN@$CsPbBr_3$ shows much faster decay after the introduction of $CsPbBr_3$. Interestingly, with respect to pure $CsPbBr_3$ at 523 nm (Fig. S16b†), the opposite trend could be observed. The results testify that the photogenerated electrons of m-CN and holes of $CsPbBr_3$ will migrate towards each other under the effect of a built-in electric field,

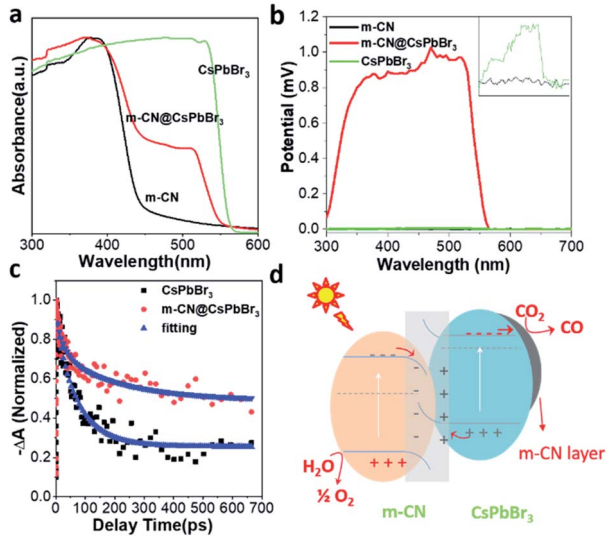

Fig. 2 (a) UV-Vis absorption spectra of m-CN@$CsPbBr_3$, the reference m-CN and $CsPbBr_3$; (b) surface photovoltage plots of the m-CN, $CsPbBr_3$ and m-CN@$CsPbBr_3$ samples; (c) transient absorption spectroscopy curves and lifetime fittings at 520 nm; (d) band structure of the m-CN@$CsPbBr_3$ heterojunction and the corresponding paths of CO_2 photo-reduction.

and the photogenerated electrons may be transported from $CsPbBr_3$ to the m-CN layer. The steady-state photovoltages (SPV) of the different samples were further compared to evidence the promoted charge separation in the m-CN@$CsPbBr_3$ heterojunction, as shown in Fig. 2b. Clearly, the samples of m-CN and $CsPbBr_3$ exhibited negligible SPV signals. Meanwhile, the m-CN@$CsPbBr_3$-5 sample demonstrated the highest positive photovoltage response compared with the other catalysts with coating layers (m-CN@$CsPbBr_3$-10 and m-CN@$CsPbBr_3$-3), suggesting that its surface is populated by a concentration of holes due to the high charge-separation efficiency (Fig. S17a†).[18a] Transient photovoltage (TPV) analysis was further carried out to study the migration dynamics of the photogenerated carriers.[18] Two obvious positive response peaks (peaks 1 and 2) can be detected from the sample of m-CN@$CsPbBr_3$ under 400 nm illumination (Fig. S17b†). Peak 1 can be assigned to a fast process related to the migration of photogenerated carriers in the built-in electric fields inside particles,[18b] and thus the stronger intensity of peak 1 of m-CN@$CsPbBr_3$ suggests that more photogenerated carriers are transported to the interface between m-CN and $CsPbBr_3$. Peak 2 is thought to arise from carrier transport between particles.[18] A further step to study the carrier transfer dynamics was to perform picosecond transient absorption spectroscopy (TA). Both the samples of bare $CsPbBr_3$ (Fig. S18a†) and m-CN@$CsPbBr_3$ (Fig. S18b†) exhibit obvious negative ground-state bleaching. Fig. 2c shows the corresponding TA kinetic plots monitored at 520 nm with a distinct difference in the delays. As listed in Table S3,† the fitted average lifetime of m-CN@$CsPbBr_3$ (197.7 ps) is much longer than that of bare $CsPbBr_3$ (77.2 ps), consistent with the above transient PL and TPV results. It is concluded that the internal electric field between m-CN and $CsPbBr_3$ would promote the carrier transfer and separation in the m-CN@$CsPbBr_3$ heterojunction.[19] According to the direction of carrier transfer and the strong built-in electric field, it can be inferred that an S-scheme heterojunction is formed between m-CN and $CsPbBr_3$.

In order to acquire stronger confirmation of the direction of carrier transfer, ultraviolet photoelectron spectroscopy (UPS) was performed to check the valence band (VB) potential and conduction band (CB) potential of the m-CN and $CsPbBr_3$ samples. The results and corresponding valence/conduction band potentials (*vs.* vacuum level) are given in Fig. S19† and Table S4.† The relative valence/conduction band positions of m-CN and $CsPbBr_3$ are shown in Fig. 2d, and they can be attributed to an S-scheme heterojunction, agreeing well with the aforementioned analysis. There is an offset of the bands of the m-CN and $CsPbBr_3$, and thus close contact between these two materials would cause band bending at the interface. Then, a built-in electric field will be formed making the m-CN and $CsPbBr_3$ centers of positive and negative charges, respectively. Moreover, the unique conduction/valence band structure of this heterojunction results in polar surfaces of m-CN (holes) and $CsPbBr_3$ (electrons). This built-in electric field would also facilitate the separation of photogenerated charges and thus suppress charge recombination.

Considering that the m-CN@$CsPbBr_3$ catalyst possesses excellent photogenerated carrier separation ability, its photo-assisted thermocatalytic CO_2 reduction activity was then investigated. We evaluated the catalytic CO_2 reduction of the samples in a flow reactor with CO_2 and H_2O vapor as the reactants, such that the H_2O would continuously pass through the catalyst bed. During the flow reaction process, light and heat were applied to the reactor. Thermogravimetric analysis (TGA) was performed to check the temperature tolerance of the m-CN@$CsPbBr_3$ catalyst in nitrogen, as shown in Fig. S20.† It indicates that the thermocatalytic CRR can take place at less than 200 °C because of the absence of any decomposition below this temperature. The instability of $CsPbBr_3$ to humidity has always been a huge obstacle for applications. The m-CN@$CsPbBr_3$ catalyst with the protection of the m-CN layer was then treated in pure water to check its chemical stability. As shown in Fig. S21a and b,† after soaking in water for ~0.5 and 17 h, there is almost no change in color; however, the bare $CsPbBr_3$ turns white after being in water for less than 1 h. The corresponding XRD results show no change from before to after the water immersion for ~0.5 and 17 h. Meanwhile, bare $CsPbBr_3$ exhibited an obvious phase transition. Additionally, the water-treated samples were checked by TEM. As shown in Fig. S22,† there is almost no change in morphology after the treatment of ~0.5 and 17 h, in accordance with the above XRD results. Fig. S23† shows the XPS results of the water-treated samples, and there are almost no changes for all the studied elements. These results suggest that m-CN@$CsPbBr_3$ exhibited superior water stability due to the m-CN encapsulation. Fig. 3a compares the CO_2 reduction activities of pristine m-CN, micro-sized $CsPbBr_3$ and m-CN@$CsPbBr_3$ under three different conditions, with our m-CN@$CsPbBr_3$ catalyst benefiting from superior durability. Under the pure simulated sunlight condition (Fig. 3a), the sample of m-

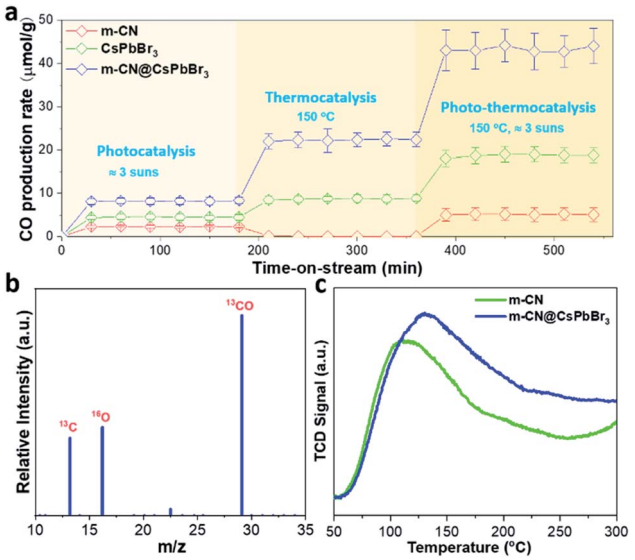

Fig. 3 (a) The CO_2 reduction to CO performance under the three conditions of photocatalysis, thermocatalysis and photo-thermocatalysis. For the latter two, the temperature is set to 150 °C; (b) mass spectrometry (MS) result of ^{13}CO produced over m-CN@$CsPbBr_3$ from the $^{13}CO_2$ isotope experiment under thermocatalysis (*m*/*z*, mass/charge ratio); (c) CO_2-TPD results of the reference m-CN and the m-CN@$CsPbBr_3$ catalyst.

CN@$CsPbBr_3$ displays the highest CO_2-to-CO yield of 8.15 μmol g^{-1} h^{-1}, followed by $CsPbBr_3$ (4.5 μmol g^{-1} h^{-1}) and m-CN (2.2 μmol g^{-1} h^{-1}). For pure thermocatalysis at the temperature of 150 °C, the CO generation of m-CN@$CsPbBr_3$ is 22.4 μmol g^{-1} h^{-1}, and those of the bare $CsPbBr_3$ and m-CN are 8.8 and 0 μmol g^{-1} h^{-1}, respectively. More impressively, when the light and heat were coupled to drive photo-assisted thermocatalysis, the CO_2-to-CO yield of m-CN@$CsPbBr_3$ was increased to 42.8 μmol g^{-1} h^{-1}, which is much higher than those of bare m-CN (5.1 μmol g^{-1} h^{-1}) and $CsPbBr_3$ (18.7 μmol g^{-1} h^{-1}). It is suggested that the light excitation would generate electrons and holes and these electrons and holes would migrate to the surfaces of $CsPbBr_3$ and m-CN, facilitating the thermocatalytic CRR process. Under all three conditions, *i.e.*, photocatalysis, thermocatalysis and photo-thermocatalysis, the sample of bare $CsPbBr_3$ gives the lowest activity, further suggesting the significance of the heterojunction for promoting the CRR performance. The photo-thermocatalytic performance of the sample of m-CN@$CsPbBr_3$ is also comparable to those of the other systems, but exceeds those of most reported $CsPbBr_3$-based photocatalysts (Table S5†). Moreover, we checked the impact of coating content on the catalytic activity of m-CN@$CsPbBr_3$ at 150 °C and 3 suns. As depicted in Fig. S24,† in comparison with m-CN@$CsPbBr_3$-3 and m-CN@$CsPbBr_3$-10, m-CN@$CsPbBr_3$-5 delivers the highest CO_2-to-CO yield, possibly due to the existence of the enriched heterogeneous interface and strong built-in electric field. Meanwhile, the catalytic stability of m-CN@$CsPbBr_3$-5 was also tested during the 6 h period of operation (Fig. S25†), and the result reveals that its reduction ability at the end is comparable to its original performance. Further, the XPS spectra before and after testing m-CN@$CsPbBr_3$-5 manifest that all elements are almost unchanged (Fig. S26†), once again verifying its excellent catalytic stability, which is promising for practical application.

In addition, a small amount of H_2 was also measured as the reductive by-product from m-CN@$CsPbBr_3$ samples at different temperatures (Fig. S27†). These results indicate that the coupling of photo and thermal effects profoundly promotes CO_2 reduction. Fig. 3b shows the result of an isotopic $^{13}CO_2$ labeling experiment under the thermocatalytic conditions. A clear peak at $m/z = 29$ (^{13}CO) is observed, confirming that the generated CO originates from the thermocatalytic reduction of $^{13}CO_2$ rather than from contaminants. The corresponding screen shots of the raw mass spectra data are displayed in Fig. S28.†

To understand the promoted performance of m-CN@$CsPbBr_3$, the adsorption abilities of CO_2 and CO on m-CN and m-CN@$CsPbBr_3$ were studied. Fig. 3c exhibits the CO_2 temperature-programmed desorption (TPD) curves of m-CN and m-CN@$CsPbBr_3$, which yield the adsorbed amounts of CO_2 according to the integrated areas of the curves. It is found that m-CN@$CsPbBr_3$ has a higher adsorbed amount and thus more sites for CO_2 adsorption and activation compared to m-CM, which could be attributed to the polar surfaces of m-CN and $CsPbBr_3$. Moreover, the desorption peak of the m-CN@$CsPbBr_3$ catalyst is situated at higher temperature, suggesting that the corresponding adsorption sites can facilitate the CO_2 reduction due to a stronger interaction with the CO_2 molecules. In the CO_2-TPD curve of $CsPbBr_3$ in Fig. S29,† a higher desorption temperature of ~320 °C is observed compared with that of m-CN, which can be responsible for the enhancement of desorption for the m-CN@$CsPbBr_3$ catalyst. CO-TPD was also performed, and the results are shown in Fig. S30.† Clearly, both the m-CN and m-CN@$CsPbBr_3$ samples showed weak CO adsorption, which is thought to benefit CO evolution. Measurements were further performed at two other temperatures (100 and 200 °C) to determine the effect of heating on the CRR efficiency. As shown in Fig. S31† (100 °C) and Fig. S32† (200 °C), the yields of CO_2-to-CO were lower than at 150 °C, which may be ascribed to the difference of CO_2 and CO adsorption at different temperatures. The result suggests that there is an optimal reaction temperature for suitable balance of adsorption/desorption of CO_2 and CO to obtain the highest performance of CO_2 reduction.

In situ FTIR spectroscopy was further carried out to investigate the possible reaction pathways of the CRR under photo-assisted thermocatalysis conditions. It is evident that increased IR peaks emerge with increasing irradiation time from 0 to 30 minutes (Fig. 4a and b), in which the peaks at 1457 cm^{-1} and 1646 cm^{-1} could be assigned to b-HCO_3^-, while the peaks at 1248 and 1695 cm^{-1} came from the vibration of the carboxylate (CO_2^-), and the peak at 1337 cm^{-1} can be attributed to the bidentate carbonate (b-CO_3^{2-}). Also, the peaks located at 1379 and 1507 cm^{-1} matched well with monodentate carbonate groups (m-CO_3^{2-}).[20] Meanwhile, for the photo-assisted thermocatalysis in Fig. 4b, almost the same peaks were observed except with relatively stronger peak intensities, corresponding to the improved CRR efficiency under the coupled photo-thermal effect. Note that the peak at 1695 increased in

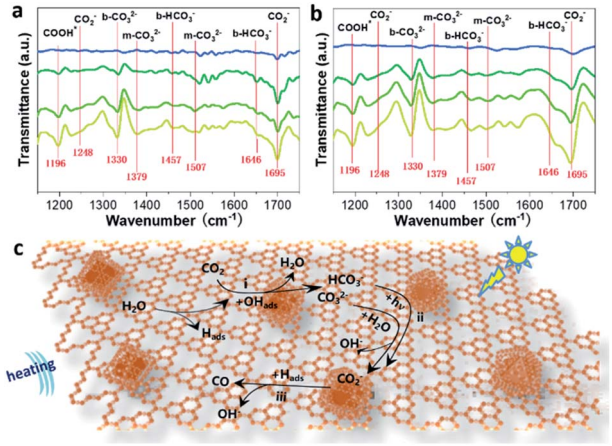

Fig. 4 *In situ* FTIR spectra of m-CN@$CsPbBr_3$ under (a) bare thermocatalytic and (b) photo-thermal conditions at ten-minute increments from 0 to 30 min (from top to bottom). (c) Schematic diagram of the possible reaction pathways of the CRR for the sample of m-CN@$CsPbBr_3$ under photo-thermal conditions.

intensity and the peaks at 1457 cm^{-1} and 1646 cm^{-1} disappeared compared with the spectrum under bare thermocatalytic conditions, indicating that b-HCO_3^- ions on the surface are transformed to surface CO_2^- species instead with the assistance of light.

In addition, the m-CO_3^{2-} signals at 1507 cm^{-1} were more obvious compared to those under bare thermocatalytic conditions, suggesting that the adsorption of the reaction intermediates was adjusted by light irradiation. This can be attributed to the strong light absorption of $CsPbBr_3$ according to the FTIR curves of the bare $CsPbBr_3$ sample under the above two conditions (Fig. S33a and b†). This finding indicates the importance of encapsulating $CsPbBr_3$ for altering the formation of intermediates and improving CRR activity under photo-assisted thermocatalysis conditions. Moreover, the FTIR curves of the reference m-CN sample are similar to those of m-CN@$CsPbBr_3$ under bare thermocatalytic conditions (Fig. S34†). Thus, the possible CRR pathways can be summarized as follows (Fig. 4c): (a) the H_2O molecules are first dissociated into H_{ads} and OH_{ads} groups when meeting hot carriers, *i.e.*, holes generated from thermal or photo excitation; (b) the adsorbed CO_2 encounters OH_{ads} to generate HCO_3^- and m-CO_3^{2-} (step i); (c) then the conversion from surface m-CO_3^{2-} (step i) to CO_2^- species in the presence of H_2O is proposed, and the surface HCO_3^- (step i) species can be converted conveniently into CO_2^- under photo-assisted thermocatalysis conditions (step ii); for (c), the CO_2^- finally releases CO gas when it encounters H_{ads} and free electrons (step iii).

Herein, a water-stable m-CN@$CsPbBr_3$ heterojunction was synthesized *via* a solid-state reaction, where bulk $CsPbBr_3$ micro-sized particles were melted and converted to nanoparticles with encapsulation by an m-CN coating during the calcination. The intimate contact between m-CN and $CsPbBr_3$ would induce band bending at the interface and form a built-in electric field, which would separate holes and electrons to m-CN and $CsPbBr_3$, respectively. As such a heterojunction with two charge poles, m-CN@$CsPbBr_3$ exhibited an excellent thermocatalytic CO_2-to-CO yield of 42.8 μmol g^{-1} h^{-1} under the assistance of irradiation, higher than that of pure photocatalysis (5.1 μmol g^{-1} h^{-1}) or thermocatalysis (18.7 μmol g^{-1} h^{-1}). This is the first report of photo-assisted thermocatalysis using $CsPbBr_3$-based materials. Our work thus expands the application of halide perovskites in CO_2 reduction.

Data availability

Experimental data have been made available as ESI.†

Author contributions

J. Y. designed this study. J. Y. and S. L. supervised and directed the experiments and reviewed and revised the manuscript. H. B. performed the experiments, analyzed the data and wrote the manuscript. D. L. and S. W. helped perform the analysis with constructive discussions.

Conflicts of interest

There are no conflicts to declare.

Acknowledgements

The authors acknowledge support from the National Key Research Program of China (2017YFA0204800), the National Natural Science Foundation of China (22072081 and 22002084), and the Fundamental Research Funds for the Central Universities (2019TS005, GK202003042, and GK202103111).

References

1 (*a*) B. Zhang and L. Sun, *Chem. Soc. Rev.*, 2019, **48**, 2216–2264; (*b*) G. Chen, G. I. N. Waterhouse, R. Shi, J. Zhao, Z. Li, L.-Z. Wu, C.-H. Tung and T. Zhang, *Angew. Chem., Int. Ed.*, 2019, **58**, 17528–17551; (*c*) H.-L. Wu, X.-B. Li, C.-H. Tung and L.-Z. Wu, *Adv. Mater.*, 2019, **31**, 1900709.

2 (*a*) A. Pan, X. Ma, S. Huang, Y. Wu, M. Jia, Y. Shi, Y. Liu, P. Wangyang, L. He and Y. Liu, *J. Phys. Chem. Lett.*, 2019, **10**, 6590–6597; (*b*) S. Shyamal, S. K. Dutta and N. Pradhan, *J. Phys. Chem. Lett.*, 2019, **10**, 7965–7969.

3 (*a*) S. Kumar, M. Regue, M. A. Isaacs, E. Freeman and S. Eslava, *ACS Appl. Energy Mater.*, 2020, **3**, 4509–4522; (*b*) A. Akhundi, A. Habibi-Yangjeh, M. Abitorabi and S. Rahim Pouran, *Catal. Rev.*, 2019, **61**, 595–628.

4 (*a*) J. Fu, K. Jiang, X. Qiu, J. Yu and M. Liu, *Mater. Today*, 2020, **32**, 222–243; (*b*) V. K. Ravi, S. Saikia, S. Yadav, V. V. Nawale and A. Nag, *ACS Energy Lett.*, 2020, **5**, 1794–1796; (*c*) Z.-C. Kong, J.-F. Liao, Y.-J. Dong, Y.-F. Xu, H.-Y. Chen, D.-B. Kuang and C.-Y. Su, *ACS Energy Lett.*, 2018, **3**, 2656–2662.

5 (*a*) Y.-F. Xu, M.-Z. Yang, B.-X. Chen, X.-D. Wang, H.-Y. Chen, D.-B. Kuang and C.-Y. Su, *J. Am. Chem. Soc.*, 2017, **139**, 5660–5663; (*b*) S. S. Bhosale, A. K. Kharade, E. Jokar, A. Fathi, S.-m. Chang and E. W.-G. Diau, *J. Am. Chem. Soc.*, 2019,

141, 20434–20442; (*c*) Z. Chen, Y. Hu, J. Wang, Q. Shen, Y. Zhang, C. Ding, Y. Bai, G. Jiang, Z. Li and N. Gaponik, *Chem. Mater.*, 2020, **32**, 1517–1525.

6 (*a*) J. Wang, J. Wang, N. Li, X. Du, J. Ma, C. He and Z. Li, *ACS Appl. Mater. Interfaces*, 2020, **12**, 31477–31485; (*b*) Y. Jiang, H.-Y. Chen, J.-Y. Li, J.-F. Liao, H.-H. Zhang, X.-D. Wang and D.-B. Kuang, *Adv. Funct. Mater.*, 2020, **30**, 2004293.

7 (*a*) B. M. Tackett, E. Gomez and J. G. Chen, *Nat. Catal.*, 2019, **2**, 381–386; (*b*) Y. Bai, J. Zhao, S. Feng, X. Liang and C. Wang, *Chem. Commun.*, 2019, **55**, 4651–4654; (*c*) X. Meng, L. Liu, S. Ouyang, H. Xu, D. Wang, N. Zhao and J. Ye, *Adv. Mater.*, 2016, **28**, 6781–6803.

8 (*a*) J. Qiao, Y. Liu, F. Hong and J. Zhang, *Chem. Soc. Rev.*, 2014, **43**, 631–675; (*b*) J. Liu, L. Zhang, D. Zang and H. Wu, *Adv. Funct. Mater.*, 2021, **31**, 2105018.

9 (*a*) L. Zhang, G. Kong, Y. Meng, J. Tian, L. Zhang, S. Wan, J. Lin and Y. Wang, *ChemSusChem*, 2017, **10**, 4709–4714; (*b*) L. Lin, K. Wang, K. Yang, X. Chen, X. Fu and W. Dai, *Appl. Catal., B*, 2017, **204**, 440–455; (*c*) Y. Wang, Q. Zhou, Y. Zhu and D. Xu, *Appl. Catal., B*, 2021, **294**, 120236.

10 (*a*) Z. Zhang, M. Shu, Y. Jiang and J. Xu, *Chem. Eng. J.*, 2021, **414**, 128889; (*b*) J.-C. Wang, N. Li, A. M. Idris, J. Wang, X. Du, Z. Pan and Z. Li, *Sol. RRL*, 2021, **5**, 2100154; (*c*) J.-F. Liao, Y.-T. Cai, J.-Y. Li, Y. Jiang, X.-D. Wang, H.-Y. Chen and D.-B. Kuang, *J. Energy Chem.*, 2021, **53**, 309–315.

11 (*a*) Q. Chen, X. Lan, Y. Ma, P. Lu, Z. Yuan and J. Shi, *Sol. RRL*, 2021, **5**, 2100186; (*b*) Y. Wang, Z. Liu, X. Tang, P. Huo, Z. Zhu, B. Yang and Z. Liu, *New J. Chem.*, 2021, **45**, 1082–1091.

12 Y.-F. Mu, W. Zhang, G.-X. Dong, K. Su, M. Zhang and T.-B. Lu, *Small*, 2020, **16**, 2002140.

13 (*a*) F. Xu, K. Meng, B. Cheng, S. Wang, J. Xu and J. Yu, *Nat. Commun.*, 2020, **11**, 4613; (*b*) Y.-F. Xu, X.-D. Wang, J.-F. Liao, B.-X. Chen, H.-Y. Chen and D.-B. Kuang, *Adv. Mater. Interfaces*, 2018, **5**, 1801015.

14 (*a*) M. Ou, W. Tu, S. Yin, W. Xing, S. Wu, H. Wang, S. Wan, Q. Zhong and R. Xu, *Angew. Chem., Int. Ed.*, 2018, **57**, 13570–13574; *Angew. Chem.*, 2018, **130**, 13758–13762; (*b*) K. Su, G.-X. Dong, W. Zhang, Z.-L. Liu, M. Zhang and T.-B. Lu, *ACS Appl. Mater. Interfaces*, 2020, **12**, 50464–50471.

15 (*a*) Q. Chen, Y. Ma, L. Wang, X. Lan and J. Shi, *Sol. RRL*, 2021, **5**, 2000755; (*b*) Y. Jiang, J.-F. Liao, H.-Y. Chen, H.-H. Zhang, J.-Y. Li, X.-D. Wang and D.-B. Kuang, *Chem*, 2020, **6**, 766–780; (*c*) J. Fu, Y. Hou, X. Liu, M. Zheng and M. Zhu, *J. Mater. Chem. C*, 2020, **8**, 8704–8731.

16 (*a*) P. Kumar, E. Vahidzadeh, U. K. Thakur, P. Kar, K. M. Alam, A. Goswami, N. Mahdi, K. Cui, G. M. Bernard, V. K. Michaelis and K. Shankar, *J. Am. Chem. Soc.*, 2019, **141**, 5415–5436; (*b*) Y. Wang, Y. Zhang, S. Zhao, Z. Huang, W. Chen, Y. Zhou, X. Lv and S. Yuan, *Appl. Catal., B*, 2019, **248**, 44–53; (*c*) S. Yang, Y. Gong, J. Zhang, L. Zhan, L. Ma, Z. Fang, R. Vajtai, X. Wang and P. M. Ajayan, *Adv. Mater.*, 2013, **25**, 2452–2456; (*d*) J. De Roo, M. Ibáñez, P. Geiregat, G. Nedelcu, W. Walravens, J. Maes, J. C. Martins, I. Van Driessche, M. V. Kovalenko and Z. Hens, *ACS Nano*, 2016, **10**, 2071–2081.

17 (*a*) X. Li, Y. Wang, H. Sun and H. Zeng, *Adv. Mater.*, 2017, **29**, 1701185; (*b*) J. Zhang, M. Zhang, L. Lin and X. Wang, *Angew. Chem., Int. Ed.*, 2015, **54**, 6297–6301; *Angew.Chem.*, 2015, **127**, 6395–6399; (*c*) D. J. Martin, K. Qiu, S. A. Shevlin, A. D. Handoko, X. Chen, Z. Guo and J. Tang, *Angew. Chem., Int. Ed.*, 2014, **53**, 9240–9245; *Angew. Chem.*, 2014, **126**, 9394–9399.

18 (*a*) X. Zhang, K. Hu, X. Zhang, W. Ali, Z. Li, Y. Qu, H. Wang, Q. Zhang and L. Jing, *Appl. Surf. Sci.*, 2019, **492**, 125–134; (*b*) C. Han, R. Zhang, Y. Ye, L. Wang, Z. Ma, F. Su, H. Xie, Y. Zhou, P. K. Wong and L. Ye, *J. Mater. Chem. A*, 2019, **7**, 9726–9735.

19 (*a*) X. Jiao, Z. Chen, X. Li, Y. Sun, S. Gao, W. Yan, C. Wang, Q. Zhang, Y. Lin, Y. Luo and Y. Xie, *J. Am. Chem. Soc.*, 2017, **139**, 7586–7594; (*b*) J. Liu, M. Liu, X. Yang, H. Chen, S. F. Liu and J. Yan, *ACS Sustainable Chem. Eng.*, 2020, **8**, 6055–6064.

20 S. Wang, X. Hai, X. Ding, S. Jin, Y. Xiang, P. Wang, B. Jiang, F. Ichihara, M. Oshikiri, X. Meng, Y. Li, W. Matsuda, J. Ma, S. Seki, X. Wang, H. Huang, Y. Wada, H. Chen and J. Ye, *Nat. Commun.*, 2020, **11**, 1149.